FRONTIERS OF PHYSICS

RESEARCH ARTICLE
Volume 19 / Issue 5 / 53206 / 2024

Van der Waals epitaxy of type-II band alignment $CsPbI_3$/TMDC heterostructure for optoelectronic applications

Chang Lu[1], Shunhui Zhang[1], Meili Chen[1], Haitao Chen[2], Mengjian Zhu[2], Zhengwei Zhang[1], Jun He[1], Lin Zhang[1,†], Xiaoming Yuan[1,‡]

1 Hunan Key Laboratory of Super Microstructure and Ultrafast Process, School of Physics, Central South University, Changsha 410083, China
2 College of Advanced Interdisciplinary Studies & Hunan Provincial Key Laboratory of Novel Nano-Optoelectronic Information Materials and Devices, National University of Defense Technology, Changsha 410073, China
Corresponding authors. E-mail: †lin.zhang@csu.edu.cn, ‡xiaoming.yuan@csu.edu.cn

Received December 9, 2024; accepted March 8, 2024

ABSTRACT

Van der Waals epitaxy allows heterostructure formation without considering the lattice match requirement, thus is a promising method to form 2D/2D and 2D/3D heterojunction. Considering the unique optical properties of $CsPbI_3$ and transition metal dichalcogenides (TMDCs), their heterostructure present potential applications in both photonics and optoelectronics fields. Here, we demonstrate selective growth of cubic phase $CsPbI_3$ nanofilm with thickness as thin as 4.0 nm and Zigzag/armchair orientated nanowires (NWs) on monolayer WSe_2. Furthermore, we show growth of $CsPbI_3$ on both transferred WSe_2 on copper grid and WSe_2 based optoelectrical devices, providing a platform for structure analysis and device performance modification. Transmission electron microscopy (TEM) results reveal the epitaxial nature of cubic $CsPbI_3$ phase. The revealed growth fundamental of $CsPbI_3$ is universal valid for other two-dimensional substrates, offering a great advantage to fabricate $CsPbI_3$ based van der Waals heterostructures (vdWHs). X-ray photoelectron spectroscopy (XPS) and optical characterization confirm the type-II band alignment, resulting in a fast charger transfer process and the occurrence of a broad emission peak with lower energy. The formation of $WSe_2/CsPbI_3$ heterostructure largely enhance the photocurrent from 2.38 nA to 38.59 nA. These findings are vital for bottom-up epitaxy of inorganic semiconductor on atomic thin 2D substrates for optoelectronic applications.

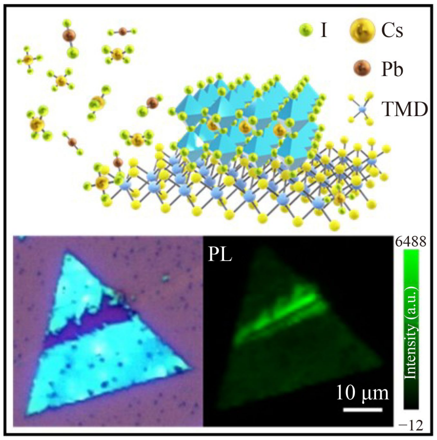

Keywords van der Waals epitaxy, band alignment, growth fundamental, charge transfer, photodetector

1 Introduction

Thanks to the discovery of two-dimensional materials with fruitful unique properties, such as boron nitride (h-BN), TMDCs and graphene, it unlocked new opportunities for next generation of electronic and optoelectronic devices such as photodetectors [1, 2], transistors [3, 4], light emitting diodes [5], lasers [6–8], and photovoltaic devices [9, 10]. Van der Waals heterostructures (vdWHs) allow easy tuning of the optical and electrical properties that are desired for specific applications. First, the formation of vdWH is a promising strategy to overcome

https://doi.org/10.1007/s11467-024-1404-9

the drawback of weak light absorption in monolayer TMDCs. Tsang *et al.* [11] designed a $PtSe_2$/CdTe heterostructure, the increased light absorption together with charge transfer improved the responsivity and on/off current ratio to 506.5 mA/W and 7 × 10^6. Secondly, vertical TMDC heterostructures with twist angle create an interfacial charge transfer pathway and allow formation of interlayer excitons with longer lifetime, thus attracting extensive attentions [12]. Thirdly, vdWH is able to enhance the Förster-type energy transfer efficiency. Kozawa *et al.* [13] exhibited efficient and ultrafast (~1 ps) fluorescence resonance energy transfer (FRET) in a closely coupled WS_2/$MoSe_2$ heterojunction, which can be applied for energy harvesting. For the purpose to improve the light absorption, inorganic metal-halide perovskite is an ideal candidate showing high light absorption coefficients, high optoelectronic conversion efficiency, thus have been widely used for low-cost and efficient photonic, photovoltaic and optoelectronic devices [14]. Benefiting from these distinct advantages, inorganic metal-halide perovskites are utilized in the formation of heterojunctions with TMDCs, resulting in a profound alteration of their optical properties as well as enhancements in device performance, such as photoelectric detection [15, 16] and light-harvesting [17].

Currently, top-down transferring is widely used to prepare inorganic metal-halide perovskite/TMDCs heterojunctions thanks to its advantages in rapid fabrication of different heterojunctions, such as quantum dots(QDs) [18] and NWs [19] on TMDCs. This method is suitable to study the optical and electronic properties of the heterostructure as well as prototype device fabrication [20–22]. By utilizing a hybrid structure consisting of metal-halide perovskites and TMDCs, it becomes possible to activate distinct nonradiative exciton relaxation (NRER) channels at the interface. Jiang *et al.* [18] demonstrated that $CsPbBr_3$ QDs/monolayer WS_2 forms a type-I band alignment, showing efficient and charge transferring process which can boost the photodetection efficiency. Moreover, MoS_2/$CsPbBr_3$ heterostructure based device shows efficient charge separation at the heterojunction interface and thus enhanced photoelectric conversion efficiency [23]. Despite the great achievement of top-down transferring approach, their applications are limited by lack of capability in scalable production. On the contrary, van der Waals epitaxy is another method of fabricating 2D material based heterostructure. Differing from traditional epitaxy, this method relies on weak van der Waals force between the 2D substrate and the epitaxial 2D or 3D layer, thus it does not need to satisfy lattice-match requirement during traditional epitaxy method [24]. Moreover, employing van der Waals epitaxy permits adjustment of crystal structure, composition and thickness of the heterostructure, further refining its photoelectric performance. Consequently, These advantages make it highly suitable for heterojunction integration, thus gathering significant attentions [25–32], such as III–V semiconductor on graphene/mica [24, 33], perovskite NWs/nanoplate on mica [34], ZnO [35], and Ga_2O_3 on mica [36]. During these studies, graphene and mica are mostly applied thanks to their easy availability as well as good heat tolerance. TMDCs are also applied for van der Waals epitaxy of free standing $In_xGa_{1-x}As$ NWs [37]. This method can enable large-scale, patterned high-quality 2D material/inorganic semiconductor heterojunction formation, rendering the van der Waals heterojunction field particularly attractive. Indeed, wafer scale high quality GaAs and GaN related heterostructure have been applied to grown on graphene (h-BN) and applied for flexible as well as vertical full-color micro-LED applications [33, 38]. Despite of these advantages, the development of van der Waals epitaxy still needs more research. Firstly, more growth fundamental should be revealed to understand its growth mechanism. Secondly, previous results mainly focus on the van der Waals epitaxy itself instead of the properties of the formed heterostructure. Thirdly, even though van der Waals epitaxy of metal-halide perovskite on mica has been reported [39], no attempts on van der Waals epitaxy of $CsPbX_3$ on TMDCs have been reported.

Considering the importance of van der Waals epitaxy in heterostructure formation and potential application in the photonic and electronic fields between TMDCs and inorganic perovskite semiconductor, we aim to bridge the gap by demonstrating the growth of $CsPbI_3$ on TMDCs layers via the chemical vapor deposition (CVD) method. We show that $CsPbI_3$ can selectively grow on WSe_2 within a wide range of growth parameters with morphology of either nanofilm or NWs. The appropriate growth temperature and precursor concentration are critical parameters for controlling the growth mode of $CsPbI_3$, deepening the van der Waals growth fundamental of $CsPbI_3$. By tuning the growth parameters, nanofilms with adjustable thicknesses from 4.0 to 11.6 nm and NWs with Zigzag and armchair orientations can be formed, and both of which exhibit epitaxial relationships with the growth substrate. Meantime, the crystal growth prefers to form a cubic phase on WSe_2 substrate and does not damage the underlying fragile monolayer WSe_2. Additionally, high resolution XPS analysis confirms the formation of the $CsPbI_3$/WSe_2 heterojunction, which exhibits a type-II band alignment characterized by a valence band offset (VBO) of 0.46 ± 0.10 eV and a conduction band offset (CBO) of 0.34 ± 0.10 eV. Optical characterizations reveal that $CsPbI_3$ and monolayer WSe_2, MoS_2, WS_2, and $MoSe_2$ form a type-II band alignment, which exhibits efficient and ultrafast charge transport. This hybrid heterostructure induces a lower energy emission peak at the shoulder of pure TMDC emission peak at low temperature. Furthermore, the revealed growth mechanism is also applicable to other two-dimensional materials, including but not limited to $MoSe_2$, MoS_2, WS_2, and h-BN. Furthermore, we successfully grow $CsPbI_3$ film directly on monolayer WSe_2

based photodetector devices. The growth of $CsPbI_3$ notably enhance the photocurrent from 2.38 to 38.59 nA and the on/off ratio from 3.14 to 16.37. Therefore, our growth findings pave the way for integrating inorganic metal-halide perovskites and 2D materials in a controllable and scalable manner through bottom-up approach.

2 Experimental methods

2.1 $CsPbI_3$/TMDCs heterostructure formation

First, monolayer TMDC was grown on Si/SiO_2 substrate via physical vapor deposition (PVD) method in a single-zone tube furnace (Jiusuo Technology) equipped with 1-inch diameter quartz tube [40]. Then, heterostructure formation is realized by growing $CsPbI_3$ in a dual-zone tube furnace with 1-inch diameter quartz tubes. A mixture of cesium iodide powder (40 μmol, 99%, Sigma-Aldrich) and lead iodide powder (40 μmol, 98%, Sigma-Aldrich) was used as precursor for $CsPbI_3$ growth and placed in the heating zone of the furnace. Before heating, the furnace was pumped to base pressure about 0.01 mbar and then a mixed Ar/H_2 with ratio of 19:1 was used as the carrier gas at a flow rate of 200 sccm until the pressure was stabilized at 400-500 mbar. The as-grown TMDC layer on SiO_2/Si substrate was put approximately 4 inches downstream from the precursor. The pressure of the furnace during the growth was controlled by a mechanical pump and measured by vacuum gauge. During the growth, the temperatures of the precursor was set at 660 °C while the growth temperature of the substrate was changed from 170–330 °C. The CVD reaction was carried out for 5 minutes followed by natural cooling down of the furnace. The standard growth temperature, precursor weight and pressure are 230 °C, 80 μmol precursor mixture and 400 mbar, respectively, since it leads to uniform $CsPbI_3$ film growth.

2.2 Device fabrication and measurement

The obtained WSe_2 films were transferred onto Si/SiO_2 substrates with PDMS thin films. The Au electrodes were fabricated on WSe_2 by photolithography and electron-beam evaporation, leading to a channel width of 2–10 μm and an electrode width of 3 μm. Subsequently, the fabricated WSe_2 device was loaded into the furnace for $CsPbI_3$ film growth. The electronic measurements were carried out in a probe station, and data were recorded with a semiconductor device analyzer (Agilent-B1500A).

2.3 Optical characterizations

The morphology of $CsPbI_3$/TMDCs heterostructures were characterized using optical microscopy, scanning electron microscopy (SEM, Tescan Mira4) and atom force microscopy (AFM, Agilent 5500 AFM/SPM). HRTEM images were recorded using a JEM-F200 microscope operated at an accelerating voltage of 80 kV to avoid damage to the $CsPbI_3$. For HRTEM characterization studies, WSe_2 was first transferred to a copper grid by a typical KOH-assisted wet-transfer method [41]. Then, $CsPbI_3$ was grown on the transferred WSe_2 before TEM analysis. XPS analyses (Thermo Scientific K-Alpha) were used to evaluate the chemical compositions and valence states of the as-grown samples. All Raman and photoluminescence (PL) measurements at room temperature were performed using a Renishaw in Via Reflex system where a 532 nm laser was focused onto the sample through a ×50 objective lens, resulting in a spot diameter of smaller than 1 μm. For temperature dependent PL measurements, LINKAM's cryogenic controller and probe stand was connected to the PL system and the laser spot was focused on the sample through a long working distance ×50 objective lens. Time-resolved photoluminescence (TRPL) were measured in a home-built micro-PL system where 532 nm pulsed laser was focused on the sample via a ×100 objective lens and the decay signal was detected by a single photon detector connected to a Picoharp 300 system [42].

3 Results and discussion

Figure 1 shows the successful growth of $CsPbI_3$ nanofilm and NWs on monolayer WSe_2. Growth temperature plays an important role in determining the morphology of $CsPbI_3$. At low temperature, such as 230 °C, $CsPbI_3$ nanofilms grow selectively on WSe_2 monolayer while no growth is observed on the SiO_2 surface. Increasing temperature to 260 °C leads to the formation of a high density of $CsPbI_3$ NWs. Further increasing the temperature to 330 °C, the surface adatom concentration of CsI and PbI_2 on WSe_2 becomes lower than that required to overcome the nucleation barrier, thus no $CsPbI_3$ crystal could be observed. However, due to the presence of dangling bonds, there is a lower nucleation barrier at the edge of WSe_2, allowing for nucleation and formation of $CsPbI_3$ triangular rings [see Fig. 1(c)]. Further increasing the temperature results in no $CsPbI_3$ nucleation on the whole substrate. It is worth mentioning that during the whole investigated temperature range from 170 °C to 330 °C [see Fig. S1 in the Supporting Information (SI)], $CsPbI_3$ prefers to selectively grow on the WSe_2 instead of the amorphous SiO_2 substrate.

Precursor concentration is another important parameter determines the growth of $CsPbI_3$. At standard film growth conditions, either lower or double the precursor weight does not change the morphology of as-grown $CsPbI_3$ except for the film thickness. Indeed, AFM

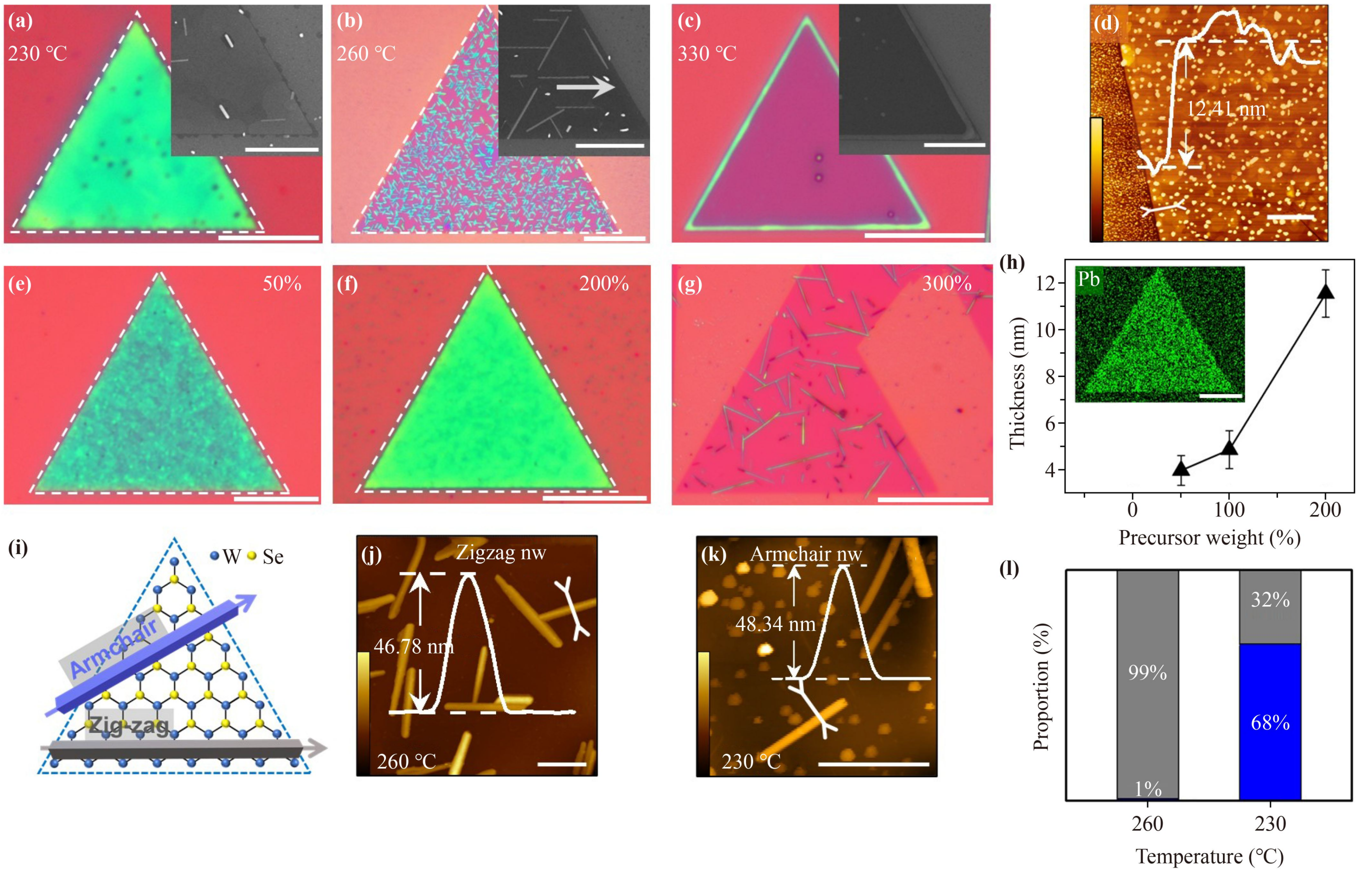

Fig. 1 Formation of $CsPbI_3$ nanostructure on monolayer WSe_2. Temperature dependent morphology evolution of $CsPbI_3$ at growth temperature of **(a)** 230 °C; **(b)** 260 °C; **(c)** 330 °C. **(d)** AFM image of a $CsPbI_3$ film. Morphology evolution of $CsPbI_3$ on monolayer WSe_2 at different precursor weight under the standardized $CsPbI_3$ film growth condition at 230 °C **(e)** 50%; **(f)** 200%; **(g)** 300%. **(h)** $CsPbI_3$ film thickness under different precursor weight. Insets are corresponding EDX mapping of Pb element. **(i)** Schematic representation of $CsPbI_3$ NWs on monolayer WSe_2 with different orientations. AFM images of $CsPbI_3$ NWs along Zigzag **(j)** and armchair **(k)** directions. **(l)** Statistics of $CsPbI_3$ NW orientation preference along Zigzag and armchair directions. Scale bars are 20 μm in (a–c, e–g), 5 μm in insets (a–c), 5 μm in (k), 2 μm in (d), 10 μm in (h), 1 μm in (j).

measurements in Fig. 1(h) demonstrate that the film thickness can be tuned from around 5 nm to ~12 nm by changing the precursor weight. Energy Dispersive X-Ray Spectroscopy (EDX) mapping shows the uniform distribution of Pb element on the WSe_2 flake, again confirming the formation of $CsPbI_3$ film. It is worth mentioning that, the $CsPbI_3$ thickness can be manipulated by changing the growth time as well (see Fig. S2 in the SI). From both inset SEM images in Figs. 1(a)–(c) and AFM images, there exist $CsPbI_3$ islands on the WSe_2, indicating that the as-grown $CsPbI_3$ film is formed by multi nucleation and growth process. Despite of the island formation, our method can selectively grow $CsPbI_3$ on WSe_2 with tunable thickness at nanometer scale, which is important to study the optical performance of the heterostructure. Surprisingly, further elevating the precursor weight ratio to threefold leads to NW formation against thick film. These formed NWs under two different growth conditions are slightly different. In general, $CsPbI_3$ NWs prefer to grow along either Zigzag or armchair direction of the WSe_2, as illustrated in Fig. 1(i). At high growth temperature, nearly all the NWs grow along the Zigzag direction with a height of around 47 nm. In comparison, the aligned direction of NWs grown at lower temperature but higher precursor weight is different. Statistically, around 68% (32%) of NWs grow along the armchair (Zigzag) direction. The NW height is measured to be around 48.3 nm. In addition to growth temperature and precursor weight, the growth pressure affects the $CsPbI_3$ growth trend as well (see Fig. S3 in the SI). Maintaining a suitable pressure is a key for successful $CsPbI_3$ film growth.

The observed growth evolution of $CsPbI_3$ is explained in Fig. 2. Supersaturation of $CsPbI_3$, which is determined by the growth temperature and the localized concentration on the WSe_2, plays a crucial role in determining the nucleation process. The growth behavior of $CsPbI_3$ is related to the adsorption, diffusion and desorption of CsI

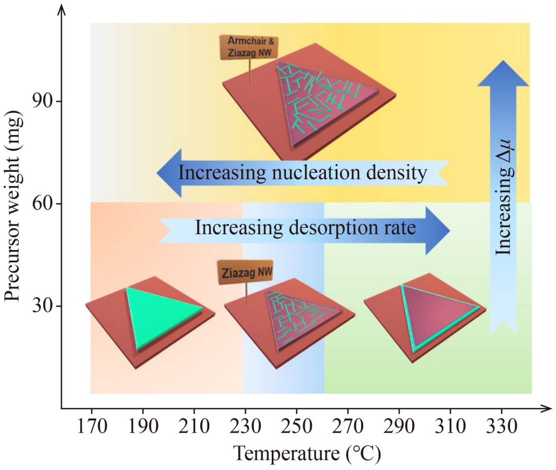

Fig. 2 Illustration of morphology evolution of $CsPbI_3$ on WSe_2 monolayer with different growth parameters.

and PbI_2 adatoms on the WSe_2. These three processes compete with each other. According to the literature [43], the low adsorption energy of CsI on TMD leads to a higher precursor concentration on the TMD than the SiO_2 substrate, thus resulting selective growth of $CsPbI_3$ on WSe_2. At low temperatures, the desorption rate of adatoms on the surface of WSe_2 is low. Consequently, the high precursor concentration on the surface exceeds what is required to overcome the nucleation barrier and leads to a high nucleation density on the whole WSe_2 flake. During growth, these nuclei continue to grow and expand, forming large polycrystal nanofilms on WSe_2. According to the well-known van der Waals growth mechanism, heterostructure with the smallest lattice match is easy to form, since the interface strain caused by lattice mismatch can be effectively reduced [44], thereby minimizing the interfacial energy. During the growth, when lattice mismatch along one certain direction is small but quite large when perpendicular to this direction, crystal thus prefers to grow along one direction to minimize the interfacial energy, thus leading to the formation of NWs [45]. Normally high precursor diffusion rate allows growth of crystal with the smallest lattice mismatch [46]. According to the calculations, lattice mismatch between $CsPbI_3$ and WSe_2 is quite small along Zigzag and armchair directions, which is 0.2% and 0.5% respectively, as shown in Fig. S4. In comparison, lattice mismatch perpendicular to Zigzag (2.3%) and armchair direction (1.3%) is quite large. At high temperatures, the elevated temperature can increase the diffusion rate of precursor and reduce the adatom concentration on the WSe_2, explaining the reduced nucleation density. Consequently, crystal prefers to grow with minimum lattice mismatch or interfacial energy. Based on our calculation, $CsPbI_3$ along Zigzag direction shows the smallest lattice match, therefore NWs are formed along Zigzag direction. At high precursor weight, it is surprising to see the formation of NWs but this trend has been double checked. It is probably that the adatom diffusion rate and desorption rate of $CsPbI_3$ precursor on the WSe_2 surface is chemical potential dependent. Since the NW along armchair and Zigzag direction both show quite small lattice mismatch, the large driving force under high precursor weight allows NWs to be formed either along Zigzag or armchair directions.

To verify the microstructure of perovskite on TMDC, we successfully developed a method to allow growth of $CsPbI_3$ on WSe_2 transferred to a copper grid. From TEM analysis, both NW like and film like $CsPbI_3$ can be observed. For the NW like shape [see Fig. 3(a)], HRTEM show the lattice distance of (200) plane is 3.15 Å, agreeing with reported value for cubic $CsPbI_3$ structure [47]. Moreover, the selected area electron diffraction (SAED) presents the same diffraction pattern as cubic phase $CsPbI_3$ along [001] zone axis. The SAED together with the HRTEM confirms that the as-grown $CsPbI_3$ NW is cubic structure and grow along [200] direction. Further EDX mapping and EDX spectrum [see Figs. 3(d, e)] again confirm the uniform distribution of Cs, Pb and I elements, verifying the successful formation of $CsPbI_3$. For the $CsPbI_3$ nanofilm in Fig. 3(f), nanofilm is grown along the [111] direction, the corresponding SADP present hexagonal shape. The measured $(0\bar{1}1)$ plane lattice distance is 4.41 Å, agreeing with the previous results. Moreover, from the DP of $CsPbI_3$ and underline WSe_2, the $(0\bar{1}1)$ plane of $CsPbI_3$ is parallel to the $(1\bar{1}0)$ direction of WSe_2, demonstrating the epitaxial nature of $CsPbI_3$ nanofilm. Figure S5(a) shows the XRD patterns of $CsPbI_3$ nanostructure. Sharp diffraction peaks at 14.1°, 40.7° and 45.5° can be observed, which are ascribed to the (100), (220) and (310) planes of the cubic $CsPbI_3$ based on the literatures [48]. The measured XRD results agree with our TEM measurement in Fig. 3(c). AFM measurements of the as-grown WSe_2 flake show the thickness of around 1 nm, demonstrating that the used WSe_2 for $CsPbI_3$ growth is actually monolayer (see Fig. S5 in the SI).

The band alignment of the $CsPbI_3/WSe_2$ heterostructure was determined using XPS, as shown in Figs. 3(i)–(l). The VBO is primarily derived by evaluating the energy discrepancy between the core levels of W 4f and Pb 4f and their respective energies relative to the valence band maximum (VBM) of $CsPbI_3$ and WSe_2. Consequently, the VBO of the heterostructures (denoted as ΔE_{V}) can be accurately calculated by applying the following equation [49]:

$$\begin{aligned}\Delta E_{\mathrm{V}} = {} & \left(E_{\mathrm{W4f}}^{\mathrm{WSe_2}} - E_{\mathrm{VBM}}^{\mathrm{WSe_2}}\right) \\ & + \left(E_{\mathrm{Pb4f}}^{\mathrm{WSe_2/CsPbI_3}} - E_{\mathrm{W4f}}^{\mathrm{WSe_2/CsPbI_3}}\right) \\ & - \left(E_{\mathrm{Pb4f}}^{\mathrm{CsPbI_3}} - E_{\mathrm{VBM}}^{\mathrm{CsPbI_3}}\right). \qquad (1)\end{aligned}$$

The first component of Eq. (1) is obtained by

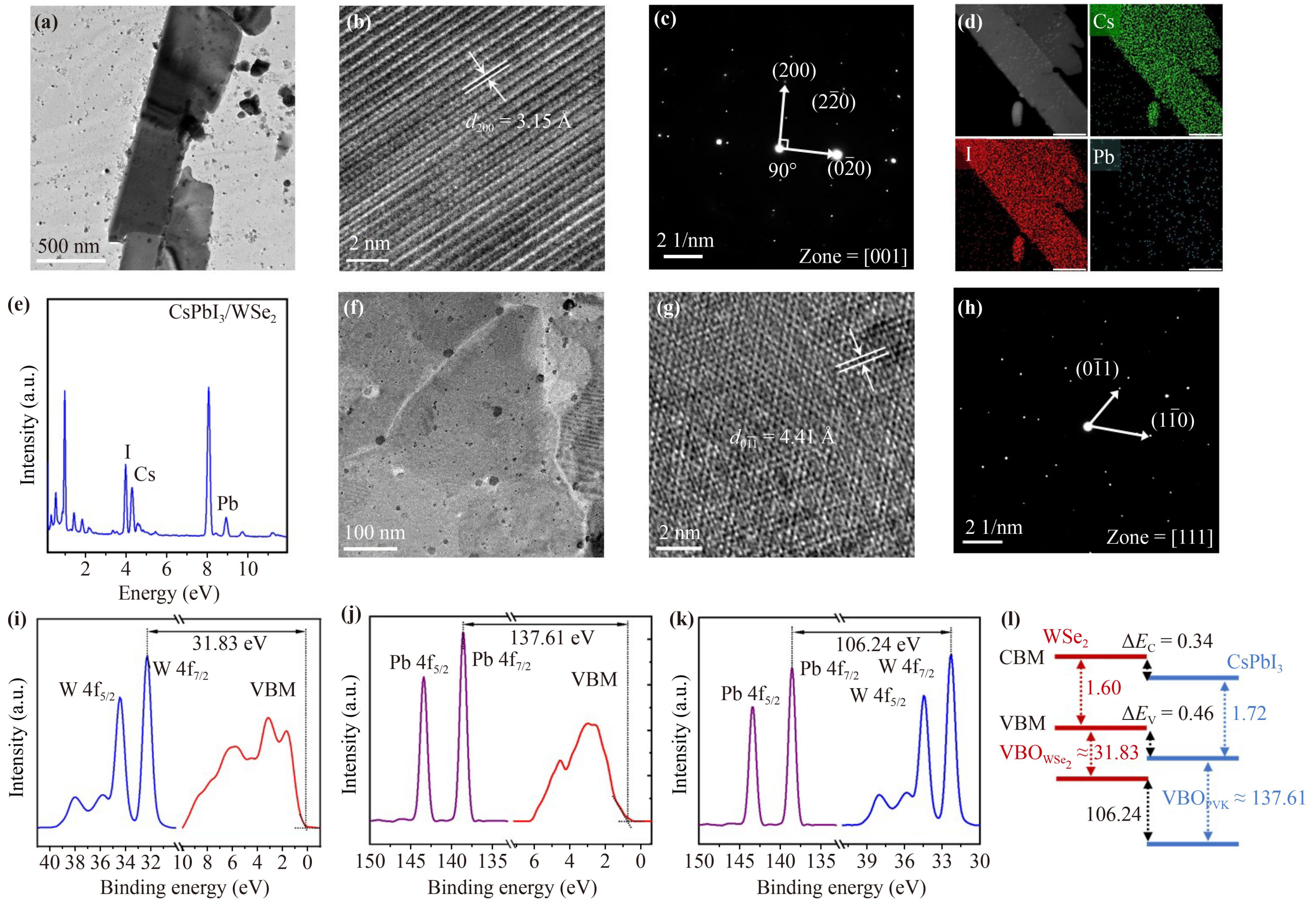

Fig. 3 Structure and band alignment of the CsPbI$_3$/WSe$_2$ heterostructure. **(a)** TEM image of a CsPbI$_3$ NW. **(b)** corresponding HRTEM image, **(c)** SAED pattern and **(d)** EDX elemental mapping **(e)** EDX spectrum of CsPbI$_3$ NW. **(f)** TEM image of CsPbI$_3$ nanofilm. **(g)** Corresponding HRTEM image and **(h)** SAED pattern of CsPbI$_3$. XPS of **(i)** W 4f core level and valence band spectra of the WSe$_2$ substrate. **(j)** Pb 4f core level and valence band spectra of CsPbI$_3$ nanostructure. **(k)** The Pb 4f and W 4f core levels in CsPbI$_3$/WSe$_2$ heterostructure. **(l)** Extracted band alignment in the CsPbI$_3$/WSe$_2$ heterostructure.

subtracting the energy difference between the W 4f$_{7/2}$ core level (32.35 ± 0.10 eV) and the VBM of WSe$_2$ [Fig. 3(i)]. The VBM of WSe$_2$ is acquired by extrapolating the linear fit to the leading edge of the valence band spectra, reaching the base level with a value of 0.52 eV. Consequently, the first component of the equation is determined to be 31.83 ± 0.10 eV. Correspondingly, the energy difference between the Pb 4f$_{7/2}$ core level (138.37 eV) and the VBM of CsPbI$_3$ (0.76 eV) is measured to be 137.61 ± 0.10 eV [Fig. 3(j)], representing the last component of the equation. The second part of the equation is calculated by computing the energy difference between the Pb 4f$_{7/2}$ and W 4f$_{7/2}$ core levels, with a value of 106.24 ± 0.10 eV [Fig. 3(k)]. Based on these results, the VBO of the CsPbI$_3$/WSe$_2$ heterojunction is determined to be 0.46 ± 0.15 eV.

The CBO (ΔE_{C}) can be then determined as follows:

$$\Delta E_{\mathrm{C}} = E_{\mathrm{g}}^{\mathrm{WSe_2}} + \Delta E_{\mathrm{V}} - E_{\mathrm{g}}^{\mathrm{CsPbI_3}}, \tag{2}$$

where $E_{\mathrm{g}}^{\mathrm{WSe_2}}$ and $E_{\mathrm{g}}^{\mathrm{CsPbI_3}}$ are the band gap of WSe$_2$ and CsPbI$_3$, respectively. The band gap is 1.72 eV for CsPbI$_3$ [50] and 1.60 eV for the WSe$_2$ [19] substrate, respectively. Based on Eq. (2), the CBO of CsPbI$_3$/WSe$_2$ heterojunction is found to be 0.34 ± 0.10 eV. The extracted band offset as shown in Fig. 3(l), demonstrating the type-II band alignment in the heterostructure.

The formation of both CsPbI$_3$ nanofilm and crystal orientation tunable NWs provides a good platform to study the optical performance of this hybrid heterostructure. CsPbI$_3$/WSe$_2$ forms a type-II band alignment [51], providing an internal electric field to separate the photogenerated electron and holes. Raman scattering comparison of WSe$_2$ before and after CsPbI$_3$ growth show unobserved difference in characteristic peak intensity, width nor peak position [see Fig. 4(a)], suggesting that van der Waals epitaxy process does not cause damage to the underline monolayer WSe$_2$ substrate thanks to the low growth temperature. For the CsPbI$_3$ NW/WSe$_2$ as well

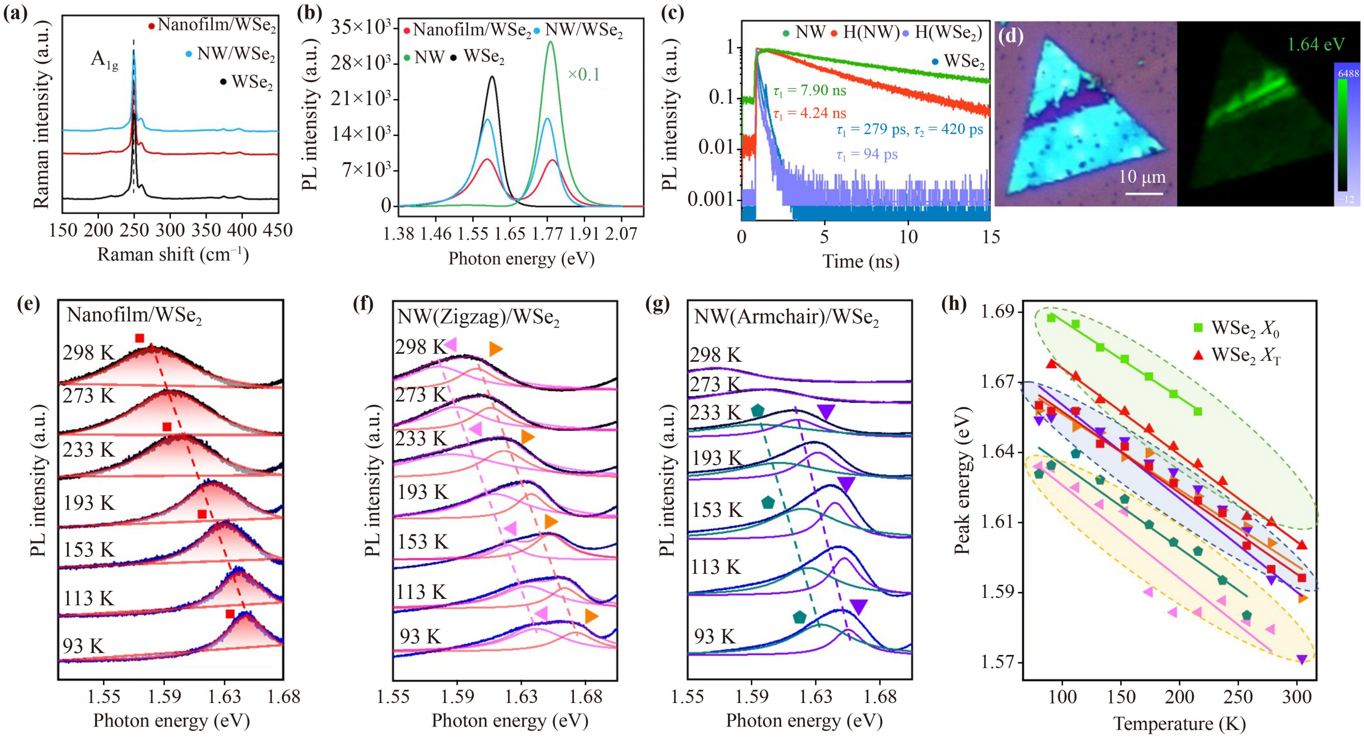

Fig. 4 **(a)** Raman spectra of monolayer WSe_2 before and after $CsPbI_3$ growth. **(b)** PL and TRPL **(c)** comparison of $CsPbI_3/WSe_2$ heterojunction, $CsPbI_3$ and WSe_2. **(d)** Optical image of a partially removed $CsPbI_3$ film on WSe_2 together with the corresponding PL mapping at 1.64 eV. **(e–g)** Temperature-dependent PL spectra of $CsPbI_3$ nanofilm/WSe_2, Zigzag orientated NW/WSe_2 and armchair orientated NW/WSe_2. **(h)** Extracted emission energy in (e–g).

as the $CsPbI_3$ nanofilm/WSe_2 heterostructure, two emission peaks corresponding to $CsPbI_3$ (1.78 eV) and WSe_2 (1.60 eV) can be observed with reduced emission intensity [see Fig. 4(b)]. Quantitatively, the emission intensity of $CsPbI_3$ is reduced over ten times. The slight emission energy shift as well as emission intensity difference between $CsPbI_3$ NW and nanofilm is ascribed to the crystal quality and thickness differences. In addition, after removing of the top $CsPbI_3$ by water washing, the emission energy as well as emission intensity is nearly unchanged, indicating that $CsPbI_3$ growth does not cause damage to the WSe_2 layer (see Fig. S7 in the SI). The corresponding TRPL decay curves in Fig. 4(c) agree with the observed PL spectra changes. The PL lifetime of isolated $CsPbI_3$ can be accurately modeled by a single-exponential function, indicating an exciton radiative recombination process [52]. The PL lifetime of pure $CsPbI_3$ NW 7.90 ns, demonstrating a high crystal quality of as-grown $CsPbI_3$ NWs [40]. After forming a heterostructure, PL lifetime is reduced to 4.24 ns, which is also ascribed to an exciton radiative recombination process. The charge transfer efficiency (ϕ_{ET}) and charge transfer rate (K_{ET}) from $CsPbI_3$ to WSe_2 can be calculated using the following equations [53, 54]:

$$\phi_{\mathrm{ET}} = 1 - \frac{\tau_{\mathrm{H}}}{\tau_{\mathrm{NW}}}, \tag{3}$$

$$K_{\mathrm{ET}} = \frac{1}{\tau_{\mathrm{H}}} - \frac{1}{\tau_{\mathrm{NW}}}, \tag{4}$$

where τ_{NW} is the PL lifetime of $CsPbI_3$ NW on the SiO_2 substrate and τ_{H} is the PL lifetime of $CsPbI_3$ NW on the monolayer WSe_2. Based on the above equations, K_{ET} and ϕ_{ET} are calculated to be 0.11×10^9 s^{-1} and 46%, respectively. The PL lifetime of monolayer WSe_2 can be effectively modeled using a biexponential function, revealing a many-body effect lifetime (τ_1) of 279 ps and an exciton radiative recombination lifetime (τ_2) of 420 ps. After forming a heterostructure, the average PL lifetime of WSe_2 is also dropped from 284 to 94 ps. K_{ET} and ϕ_{ET} are calculated to be 0.71×10^8 s^{-1} and 67%, respectively. Therefore, we believe that the observed decreased PL intensity as well as PL lifetime are explained by the fast and efficient charge transfer process due to the formed type-II band alignment.

It is worth mentioning that the observed PL and TRPL trend is valid for both $CsPbI_3$ NW and nanofilm [54]. We further performed PL intensity mapping at 1.64 eV on a $CsPbI_3/WSe_2$ heterojunction. Before measurement, the as-grown $CsPbI_3$ film is partially removed by scratching with a tweezer, exposing the underline WSe_2 [see Fig. 4(d)]. The PL intensity of the WSe_2 at the crack location is much brighter while the other region shows weak and uniform emission. This emission distribution confirms that the $CsPbI_3$ film does

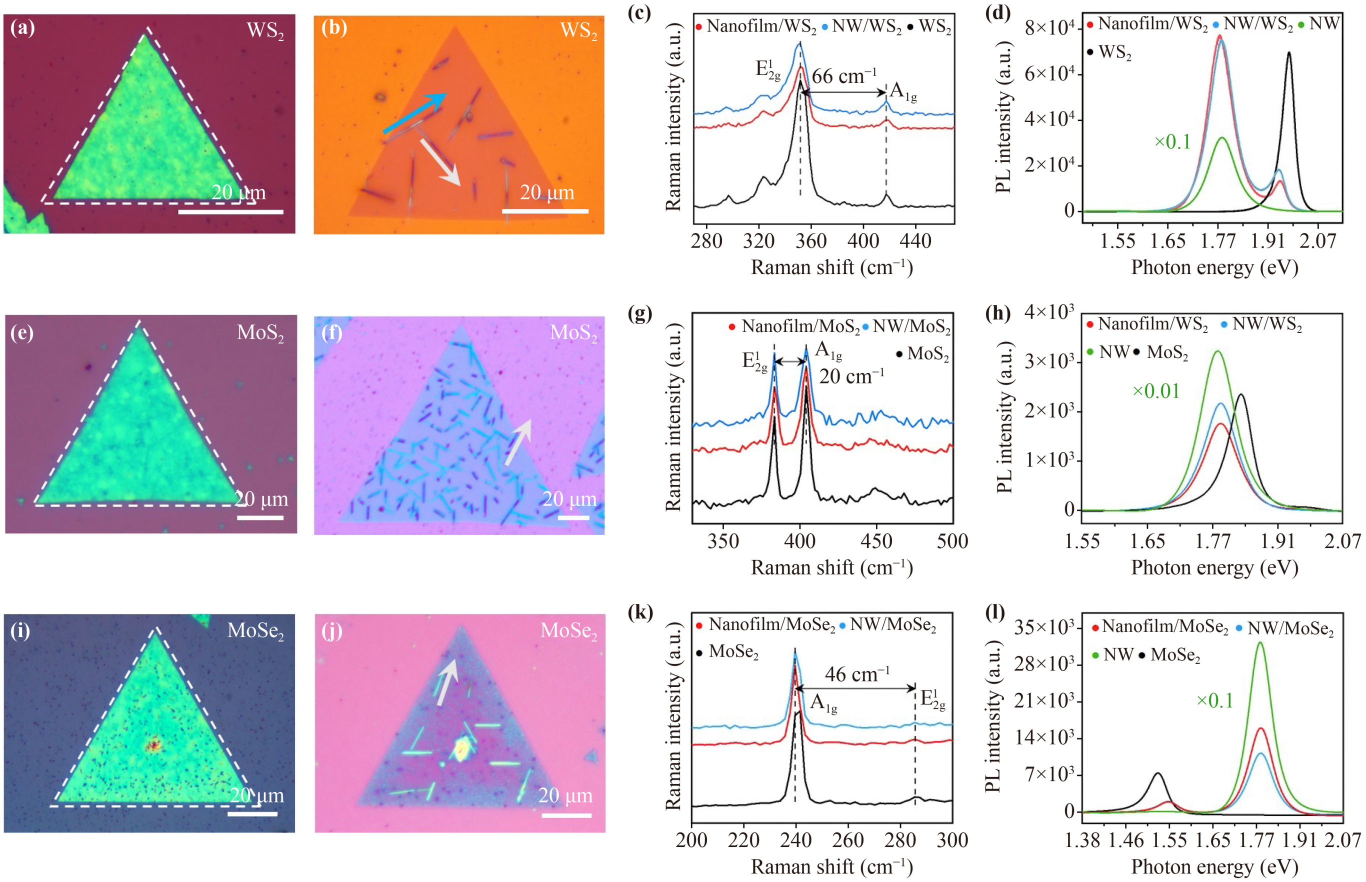

Fig. 5 Growth demonstration of CsPbI$_3$ nanofilm and NWs on monolayer WS$_2$, MoS$_2$ and MoSe$_2$ monolayer at standard film growth conditions and NW growth conditions at triple precursor weight. Optical images of CsPbI$_3$ nanofilms **(a, e, i)** and NWs **(b, f, j)** on monolayer TMDCs. Corresponding Raman **(c, g, k)** and PL **(d, h, l)** spectra of the as-grown CsPbI$_3$/ TMDCs heterojunction.

not reduce the quality of WSe$_2$ and the reduction of PL emission is definitely a result of heterostructure formation. The inherent characteristics of the two-dimensional structure, combined with the heightened Coulomb interaction, give rise to profound excitonic effects within the monolayers. Furthermore, the Coulomb interaction facilitates the preferential formation of trions alongside excitons, which frequently exhibit dominance in the PL spectra in the presence of freely mobile charges [55]. Further temperature dependent PL experiments are carried out from 300 K to 93 K. During cooling down process, the emission peak of CsPbI$_3$ gradually becomes stronger and the emission energy undergoes a redshift (Fig. S8 in the SI), agreeing with previous reports [56–59]. Below 93 K, the emission intensity of CsPbI$_3$ is so strong that the emission peak from WSe$_2$ becomes hard to distinguish. In comparison, the emission evolution of WSe$_2$ peak at heterojunction and pure WSe$_2$ flakes are compared in Figs. 4(f)–(h). In general, the emission of WSe$_2$/CsPbI$_3$ has a lower emission energy and much broader emission peak. During cooling down, the emission peak undergoes a blueshift with enhanced emission intensity. For the CsPbI$_3$ film/WSe$_2$, it presents a broad emission peak with energy linearly shifted from 1.58 to 1.65 eV during 300 to 93 K, which is around 12 meV smaller than the trion emission of WSe$_2$. For the CsPbI$_3$ NW/WSe$_2$, a low energy peak occurs at temperature below 273 K and becomes stronger during cooling down. Since the laser spot diameter is larger than the NW diameter, the emission consists of pure WSe$_2$ (higher energy peak) and heterostructure (lower energy shoulder). The exact position of the low energy peak is sample dependent and is always lower than the trion emission of WSe$_2$ [see Fig. 4(h)]. Moreover, after removing of the CsPbI$_3$ by water washing, no such a low energy emission peak is observed (see Fig. S9 in the SI), demonstrating that this low energy peak is not caused by the doping or damage of the TMDCs during CsPbI$_3$ epitaxy. Consequently, this emission is ascribed to the band alignment of the CsPbI$_3$/WSe$_2$ heterostructure.

To test whether the revealed van der Waals growth fundamental of CsPbI$_3$ is only valid for WSe$_2$ or universal valid for other 2D materials, we tried to grow CsPbI$_3$ nanofilm and NWs on monolayer WS$_2$, MoS$_2$ and MoSe$_2$

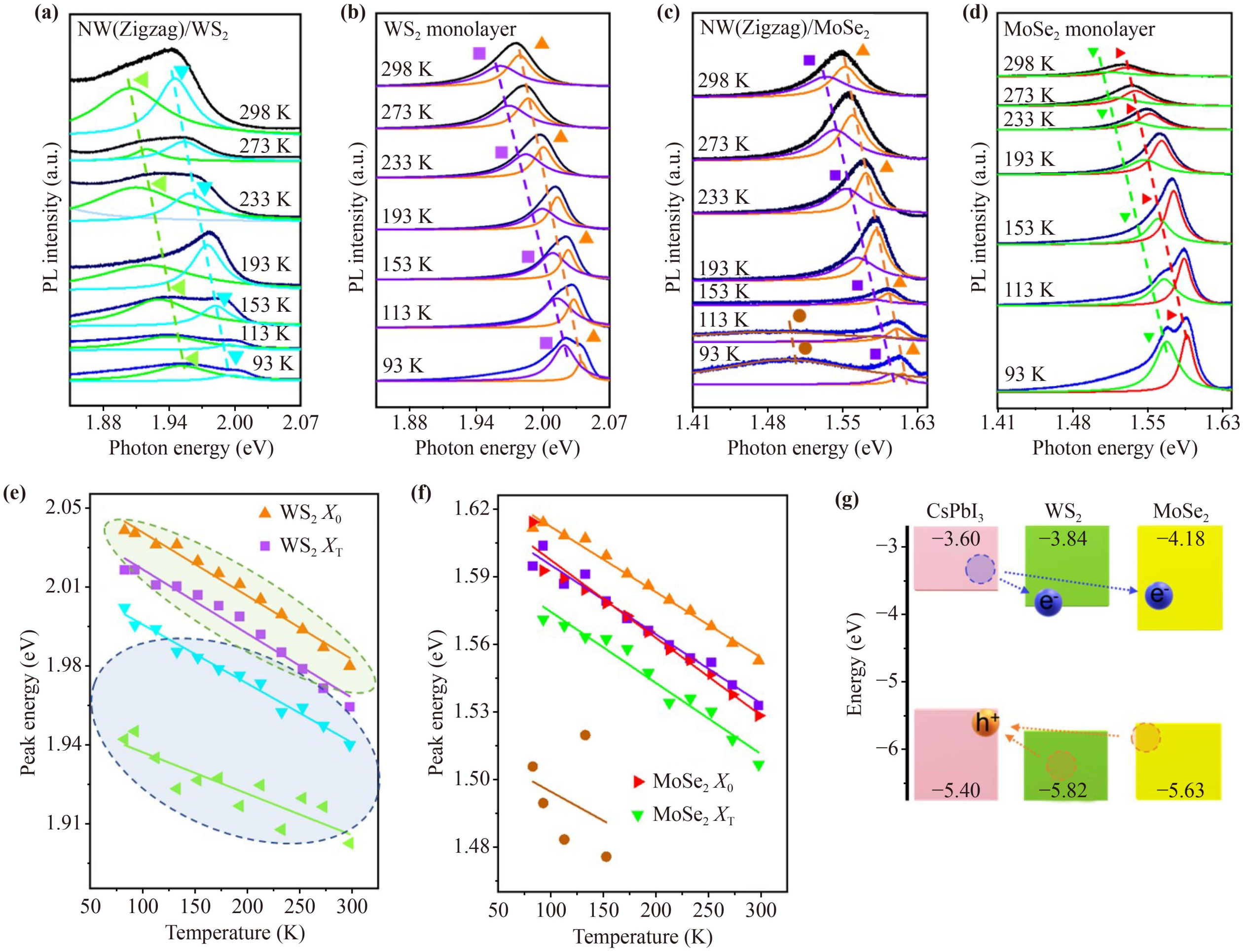

Fig. 6 **(a, b)** Temperature-dependent PL spectra of CsPbI$_3$/WS$_2$ heterojunction and monolayer WS$_2$. **(c, d)** Temperature-dependent PL spectra of CsPbI$_3$/MoSe$_2$ heterojunction and monolayer MoSe$_2$. **(e, f)** Extracted peak energy evolution with temperature for CsPbI$_3$/WS$_2$ and CsPbI$_3$/MoSe$_2$ heterojunction **(g)** Band alignments of between CsPbI$_3$ and monolayer TMDC [19]. The arrows point out the possible charge transfer process at the heterojunction.

at the same growth conditions as those on monolayer WSe$_2$. As displayed by the optical images in Fig. 5, CsPbI$_3$ nanofilms are selectively formed on TMDCs under the same growth conditions. For CsPbI$_3$ NW/TMDC heterojunction, NWs are formed on TMDCs with different density and length. The general geometric relationship between the NW and the TMDCs layer is the same, most of the NWs grow along the Zigzag direction with the rest along armchair directions. Indeed, we also successfully grow CsPbI$_3$ on multilayer WSe$_2$, transferred WSe$_2$ as well as multilayer h-BN using the standard film growth condition (see Fig. S10 in the SI). These results demonstrate that the revealed growth fundamental of CsPbI$_3$ is nearly independent on the physical properties of the underline 2D materials but is universal valid. This unique growth behavior of CsPbI$_3$ provides an advantage of forming different types of CsPbI$_3$/2D material heterojunction as demanded, which is highly suitable for novel optoelectronic device applications.

Similar to those CsPbI$_3$/WSe$_2$ heterojunction, no change could be observed for Raman scattering of monolayer TMDCs before and after CsPbI$_3$ growth. PL quenching is also observed for all the CsPbI$_3$/TMDC heterojunction, especially for the monolayer WS$_2$ related heterojunction. Slightly peak shift is observed, since trion emission is sensitive to the dielectric environment. These results suggest the CsPbI$_3$ forms a type-II band alignment with all the monolayer TMDCs. Consequently, the internal electric field induces fast carrier transfer in these heterojunctions, thus reducing the recombination chance of photoexcited electrons and holes.

The optical emission of CsPbI$_3$/TMDC are further studied at low temperature, as shown in Fig. 6 Similar to CsPbI$_3$/WSe$_2$ heterostructure, CsPbI$_3$/WS$_2$ and CsPbI$_3$/MoSe$_2$ also show similar emission behaviors. When compared with pure WS$_2$ and MoSe$_2$, a broad and low energy emission peak is always observed as a shoulder to TMDCs emission peak. The extracted peak energy evolution with temperature is shown in Figs. 6(e, f) together with the evolution of trion and exciton for pure

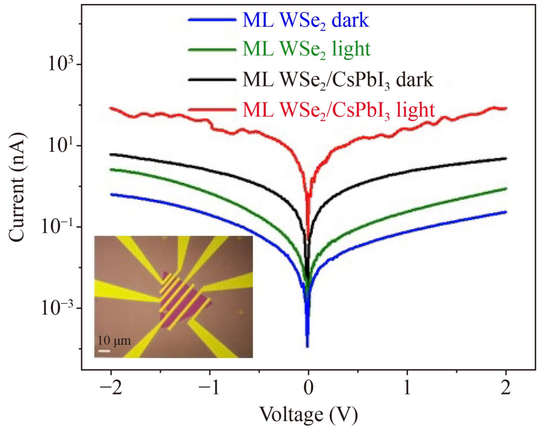

Fig. 7 Dark and photocurrent comparison of the WSe$_2$ based photodetector before and after CsPbI$_3$ growth. The inset is optical image of the as-fabricated CsPbI$_3$/WSe$_2$ device.

WS$_2$ and MoSe$_2$. For pure WS$_2$ and MoSe$_2$, trion and exciton emission shows a linear blueshift with decreasing temperature. In the case of the CsPbI$_3$ NW/WS$_2$ heterojunction, a low-energy peak is observable during the whole investigated temperature range. When temperature is below 153K, this low energy peak even outweighs the emission of pure WS$_2$. The lowest emission energy is around 80 meV lower than the trion emission of WS$_2$. It is worth mentioning that CsPbI$_3$/WS$_2$ heterojunction induced emission energy (1.93 eV) is still larger than that of CsPbI$_3$. Based on the band alignment between CsPbI$_3$ and TMDC layers in Fig. 6(g) [19], even though the heterostructure is supposed to induce a type-II emission with lower energy, this energy should be smaller than the bandgap of both CsPbI$_3$ and TMDC. Therefore, the observed lower emission energy peak in WS$_2$/CsPbI$_3$ is not related to the type-II band alignment. In terms of CsPbI$_3$ NW/MoSe$_2$ heterojunction, a low-energy peak at around 1.48 eV is observed when temperature is below 153 K. This peak energy is 72 meV lower than the trion emission of MoSe$_2$. At low temperature, the emission of CsPbI$_3$ and MoS$_2$ overlap with each other, thus is not shown here.

In all, for all the fabricated CsPbI$_3$/monolayer TMDC, it forms a type-II band alignment, which leads to a drop of PL emission due to fast charge transfer. At low temperature, band misalignment induced PL emission is not observed, probably because photo induced charges can diffuse in CsPbI$_3$, which reduce the possibility of forming interlayer exciton at the interface as those in pure TMDC heterostructure [56]. Instead, the fabricated heterostructure change the emission behavior of TMDC layer. Firstly, the dominant emission at room temperature is changed from exciton to trion, leading to a redshift of the PL emission spectrum. Secondly, a broad emission peak with energy around several tens meV lower than the trion emission can be observed, which is not aroused by defects as well as band alignment. Instead, it is supposed that this band alignment induced charge injection from CsPbI$_3$ to TMDCs layer alter the recombination paths in TMDCs. Consequently, this emission energy and intensity is sensitive to the CsPbI$_3$.

The determined type-II band alignment together with the ability to re-grown CsPbI$_3$ on transferred TMDC, suggesting that this method is able to enhance the photodetection performance of TMDC based photodetector. Thus, after metal contact to the monolayer WSe$_2$ (see optical image in the inset of Fig. 7), CsPbI$_3$ film was regrown on the fabricated WSe$_2$ devices. The I– V curves before and after CsPbI$_3$ growth are compared in Fig. 7 with a radiation of a 532 nm laser. The growth of CsPbI$_3$ significantly enhance the dark current, because the grown CsPbI$_3$ increase the dark current, which is in agreement with previous WSe$_2$–CH$_3$NH$_3$PbI$_3$ heterostructure devices [60]. The photocurrent and on/off ratio are also largely enhanced as well under all the applied voltage range. Specifically, photocurrent increases from 2.38 to 38.59 nA and the on/off ratio of CsPbI$_3$/WSe$_2$ increases from 3.14 to 16.37 under voltage of −1 V. The enhancement of optoelectronic performance agrees with our expectation, since the CsPbI$_3$ shows large light absorption coefficients and the fast charge transfer process can increase the photoinduced carrier density and thus the photocurrent. The photo response characteristics indicate that the hybrid CsPbI$_3$/WSe$_2$ possesses a great potential in the application of photodetectors.

4 Conclusions

In summary, we demonstrate direct van der Waals epitaxy of CsPbI$_3$ NWs and thickness tunable CsPbI$_3$ nanofilms on WSe$_2$ without causing any damage to the monolayer WSe$_2$ substrate. The low adsorption energy of CsI and PbI$_2$ adatoms on TMDC substrate make it possible to selectively grow CsPbI$_3$ on TMDC layer instead of the amorphous SiO$_2$ substrate. Moreover, the temperature dependent desorption rate of the precursor leads to possibility of controlling the morphology of CsPbI$_3$ from nanofilm to Zigzag/armchair orientated NWs. Both the CsPbI$_3$ nanofilm and NWs display a distinct inclination towards the formation of a cubic phase structure, establishing an epitaxial relationship with the growth substrate. The revealed van der Waals growth fundamental of CsPbI$_3$ is valid for all the TMDC layers, including but not limited to CVD grown monolayer/multilayer TMDC as well as h-BN, which pose great feasibility to design CsPbI$_3$ based van der Waals heterostructure for different application purpose. Further XPS and optical characterization confirms the type-II band alignment between CsPbI$_3$/monolayer TMDC, thus leading to a fast charge transfer process and the resulted reduction of PL emission intensity. Also, the band alignment induced carrier injection seems alters the recombination paths in TMDC monolayer, leading to the occurrence of a broad PL peak at lower energy side of pure TMDC emission. The $WSe_2/CsPbI_3$ heterostructure photodetectors exhibit enhanced photocurrent and on/off ratio. Therefore, our finding suggests a new approach to alter the emission as well as optoelectrical performance in TMDC layer.

Declarations The authors declare that they have no competing interests and there are no conflicts.

Supporting Information The online version contains the additional experiment with formation of $CsPbI_3/WSe_2$ heterostructure under altered parameters, temperature-dependent PL spectra of $CsPbI_3$ armchair orientated NW/WSe_2, formation and PL spectra of $CsPbI_3$ nanostructure on the surface of transferred hBN and DL-WSe_2, and so on (PDF). See: https://doi.org/10.1007/s11467-024-1404-9 and https://journal.hep.com.cn/fop/EN/10.1007/s11467-024-1404-9.

Acknowledgements This work was supported by the National Natural Science Foundation of China (Grant Nos. 61974166 and 62274184) and the Hunan Provincial Natural Science Foundation of China (Grant Nos. 2021JJ20080 and 2021JJ20077).

References

1. M. Long, P. Wang, H. Fang, and W. Hu, Progress, challenges, and opportunities for 2D material based photodetectors, *Adv. Funct. Mater.* 29(19), 1803807 (2019)
2. N. Huo and G. Konstantatos, Recent progress and future prospects of 2D-based photodetectors, *Adv. Mater.* 30(51), 1801164 (2018)
3. S. B. Mitta, M. S. Choi, A. Nipane, F. Ali, C. Kim, J. T. Teherani, J. Hone, and W. J. Yoo, Electrical characterization of 2D materials-based field-effect transistors, *2D Mater.* 8(1), 012002 (2021)
4. Z. Wang, Y. Yang, B. Hua, and Q. Ji, Synthetic two-dimensional electronics for transistor scaling, *Front. Phys.* 18(6), 63601 (2023)
5. J. F. Gonzalez Marin, D. Unuchek, Z. Sun, C. Y. Cheon, F. Tagarelli, K. Watanabe, T. Taniguchi, and A. Kis, Room-temperature electrical control of polarization and emission angle in a cavity-integrated 2D pulsed LED, *Nat. Commun.* 13(1), 4884 (2022)
6. K. F. Mak and J. Shan, Photonics and optoelectronics of 2D semiconductor transition metal dichalcogenides, *Nat. Photonics* 10(4), 216 (2016)
7. S. Wu, S. Buckley, J. R. Schaibley, L. Feng, J. Yan, D. G. Mandrus, F. Hatami, W. Yao, J. Vučković, A. Majumdar, and X. Xu, Monolayer semiconductor nanocavity lasers with ultralow thresholds, *Nature* 520(7545), 69 (2015)
8. Y. Ye, Z. J. Wong, X. Lu, X. Ni, H. Zhu, X. Chen, Y. Wang, and X. Zhang, Monolayer excitonic laser, *Nat. Photonics* 9(11), 733 (2015)
9. M. Bernardi, M. Palummo, and J. C. Grossman, Extraordinary sunlight absorption and one nanometer thick photovoltaics using two-dimensional monolayer materials, *Nano Lett.* 13(8), 3664 (2013)
10. C. K. Sumesh, Towards efficient photon management in nanostructured solar cells: Role of 2D layered transition metal dichalcogenide semiconductors, *Sol. Energy Mater. Sol. Cells* 192, 16 (2019)
11. D. Wu, Y. Wang, L. Zeng, C. Jia, E. Wu, T. Xu, Z. Shi, Y. Tian, X. Li, and Y. H. Tsang, Design of 2D layered $PtSe_2$ heterojunction for the high-performance, room-temperature, broadband, infrared photodetector, *ACS Photonics* 5(9), 3820 (2018)
12. L. Zhang, Z. Zhang, F. Wu, D. Wang, R. Gogna, S. Hou, K. Watanabe, T. Taniguchi, K. Kulkarni, T. Kuo, S. R. Forrest, and H. Deng, Twist-angle dependence of moiré excitons in $WS_2/MoSe_2$ heterobilayers, *Nat. Commun.* 11(1), 5888 (2020)
13. D. Kozawa, A. Carvalho, I. Verzhbitskiy, F. Giustiniano, Y. Miyauchi, S. Mouri, A. Castro Neto, K. Matsuda, and G. Eda, Evidence for fast interlayer energy transfer in $MoSe_2/WS_2$ heterostructures, *Nano Lett.* 16(7), 4087 (2016)
14. A. Liu, H. Zhu, S. Bai, Y. Reo, T. Zou, M. G. Kim, and Y. Y. Noh, High-performance inorganic metal halide perovskite transistors, *Nat. Electron.* 5(2), 78 (2022)
15. R. Singh, P. Singh, and G. Balasubramanian, Effect of heterostructure engineering on electronic structure and transport properties of two-dimensional halide perovskites, *Comput. Mater. Sci.* 200, 110823 (2021)
16. A. G. Ricciardulli, S. Yang, J. H. Smet, and M. Saliba, Emerging perovskite monolayers, *Nat. Mater.* 20(10), 1325 (2021)
17. S. S. Lo, T. Mirkovic, C. H. Chuang, C. Burda, and G. D. Scholes, Emergent properties resulting from type-II band alignment in semiconductor nanoheterostructures, *Adv. Mater.* 23(2), 180 (2011)
18. Y. Liu, H. Li, X. Zheng, X. Cheng, and T. Jiang, Giant photoluminescence enhancement in monolayer WS_2 by energy transfer from $CsPbBr_3$ quantum dots, *Opt. Mater. Express* 7(4), 1327 (2017)
19. Q. Fang, Q. Shang, L. Zhao, R. Wang, Z. Zhang, P. Yang, X. Sui, X. Qiu, X. Liu, Q. Zhang, and Y. Zhang, Ultrafast charge transfer in perovskite nanowire/2D transition metal dichalcogenide heterostructures, *J. Phys. Chem. Lett.* 9(7), 1655 (2018)
20. M. Zhong, B. Cui, Z. Mo, Y. Yu, Q. Xia, F. Zhang, Z. Zhou, L. Huang, B. Li, and J. Yang, Gate controllable band alignment transition in 2D black-arsenic/WSe_2 heterostructure, *Appl. Phys. Rev.* 10(2), 021416 (2023)
21. F. Zhao, D. Wang, F. Zhang, B. Cui, Q. Xia, and M. Zhong, Gate-controlled photoresponse improvement in b-AsP/WSe_2 heterostructures with type-I band alignment, *Appl. Phys. Lett.* 122(15), 151105 (2023)
22. L. Yuan, Z. Xu, J. Li, F. Zhang, S. Liu, H. Shi, Q. Xia, and M. Zhong, Broad-spectrum and ultrasensitive photodetectors based on $GeSe/SnS_2$ heterostructures with type-III band alignment, *Appl. Phys. Lett.* 122(24), 241106 (2023)
23. X. Song, X. Liu, D. Yu, C. Huo, J. Ji, X. Li, S. Zhang, Y. Zou, G. Zhu, Y. Wang, M. Wu, A. Xie, and H. Zeng, Boosting two-dimensional $MoS_2/CsPbBr_3$ photodetectors

via enhanced light absorbance and interfacial carrier separation, *ACS Appl. Mater. Interfaces* 10(3), 2801 (2018)

24. A. G. Saraswathy Vilasam, P. K. Prasanna, X. Yuan, Z. Azimi, F. Kremer, C. Jagadish, S. Chakraborty, and H. H. Tan, Epitaxial growth of GaAs nanowires on synthetic mica by metal–organic chemical vapor deposition, *ACS Appl. Mater. Interfaces* 14(2), 3395 (2022)
25. L. Britnell, R. M. Ribeiro, A. Eckmann, R. Jalil, B. D. Belle, A. Mishchenko, Y. J. Kim, R. V. Gorbachev, T. Georgiou, S. V. Morozov, A. N. Grigorenko, A. K. Geim, C. Casiraghi, A. H. C. Neto, and K. S. Novoselov, Strong light–matter interactions in heterostructures of atomically thin films, *Science* 340(6138), 1311 (2013)
26. Z. Liu, L. Song, S. Zhao, J. Huang, L. Ma, J. Zhang, J. Lou, and P. M. Ajayan, Direct growth of graphene/hexagonal boron nitride stacked layers, *Nano Lett.* 11(5), 2032 (2011)
27. W. Yang, G. Chen, Z. Shi, C. C. Liu, L. Zhang, G. Xie, M. Cheng, D. Wang, R. Yang, D. Shi, K. Watanabe, T. Taniguchi, Y. Yao, Y. Zhang, and G. Zhang, Epitaxial growth of single-domain graphene on hexagonal boron nitride, *Nat. Mater.* 12(9), 792 (2013)
28. M. Wang, S. K. Jang, W. J. Jang, M. Kim, S. Y. Park, S. W. Kim, S. J. Kahng, J. Y. Choi, R. S. Ruoff, Y. J. Song, and S. Lee, A platform for large-scale graphene electronics – CVD growth of single-layer graphene on CVD-grown hexagonal boron nitride, *Adv. Mater.* 25(19), 2746 (2013)
29. X. Duan, C. Wang, J. C. Shaw, R. Cheng, Y. Chen, H. Li, X. Wu, Y. Tang, Q. Zhang, A. Pan, J. Jiang, R. Yu, Y. Huang, and X. Duan, Lateral epitaxial growth of two-dimensional layered semiconductor heterojunctions, *Nat. Nanotechnol.* 9(12), 1024 (2014)
30. C. Huang, S. Wu, A. M. Sanchez, J. J. P. Peters, R. Beanland, J. S. Ross, P. Rivera, W. Yao, D. H. Cobden, and X. Xu, Lateral heterojunctions within monolayer $MoSe_2$–WSe_2 semiconductors, *Nat. Mater.* 13(12), 1096 (2014)
31. M. Chen, R. Chang, X. Yang, C. Lu, S. Zhang, Z. Zhang, J. He, and X. Yuan, Van der Waals epitaxy of $CsPbBr_3$/WSe_2 heterostructure and dynamics study of exciton recombination, *J. Phys. D Appl. Phys.* 57(23), 235103 (2024)
32. Y. H. Mao, H. Shan, J. R. Wu, Z. J. Li, C. Z. Wu, X. F. Zhai, A. D. Zhao, and B. Wang, Observation of pseudogap in $SnSe_2$ atomic layers grown on graphite, *Front. Phys.* 15(4), 43501 (2020)
33. Y. Kim, S. S. Cruz, K. Lee, B. O. Alawode, C. Choi, Y. Song, J. M. Johnson, C. Heidelberger, W. Kong, S. Choi, K. Qiao, I. Almansouri, E. A. Fitzgerald, J. Kong, A. M. Kolpak, J. Hwang, and J. Kim, Remote epitaxy through graphene enables two-dimensional material-based layer transfer, *Nature* 544(7650), 340 (2017)
34. J. Chen, Y. Fu, L. Samad, L. Dang, Y. Zhao, S. Shen, L. Guo, and S. Jin, Vapor-phase epitaxial growth of aligned nanowire networks of cesium lead halide perovskites ($CsPbX_3$, X = Cl, Br, I), *Nano Lett.* 17(1), 460 (2017)
35. S. Ge, F. Huang, J. He, Z. Xu, Z. Sun, X. Han, C. Wang, L. B. Huang, and C. Pan, Bidirectional photoresponse in perovskite-ZnO heterostructure for fully optical-controlled artificial synapse, *Adv. Opt. Mater.* 10(11), 2200409 (2022)
36. B. R. Tak, V. Gupta, A. K. Kapoor, Y. H. Chu, and R. Singh, Wearable gallium oxide solar-blind photodetectors on muscovite mica having ultrahigh photoresponsivity and detectivity with added high-temperature functionalities, *ACS Appl. Electron. Mater.* 1(11), 2463 (2019)
37. P. K. Mohseni, A. Behnam, J. D. Wood, C. D. English, J. W. Lyding, E. Pop, and X. Li, $In_xGa_{1-x}As$ nanowire growth on graphene: van der Waals epitaxy induced phase segregation, *Nano Lett.* 13(3), 1153 (2013)
38. J. Shin, H. Kim, S. Sundaram, J. Jeong, B. I. Park, C. S. Chang, J. Choi, T. Kim, M. Saravanapavanantham, K. Lu, S. Kim, J. M. Suh, K. S. Kim, M. K. Song, Y. Liu, K. Qiao, J. H. Kim, Y. Kim, J. H. Kang, J. Kim, D. Lee, J. Lee, J. S. Kim, H. E. Lee, H. Yeon, H. S. Kum, S. H. Bae, V. Bulovic, K. J. Yu, K. Lee, K. Chung, Y. J. Hong, A. Ougazzaden, and J. Kim, Vertical full-colour micro-LEDs via 2D materials-based layer transfer, *Nature* 614(7946), 81 (2023)
39. Y. Wang, Y. Shi, G. Xin, J. Lian, and J. Shi, Two-dimensional van der Waals epitaxy kinetics in a three-dimensional perovskite halide, *Cryst. Growth Des.* 15(10), 4741 (2015)
40. Z. Zhang, P. Chen, X. Yang, Y. Liu, H. Ma, J. Li, B. Zhao, J. Luo, X. Duan, and X. Duan, Ultrafast growth of large single crystals of monolayer WS_2 and WSe_2, *Natl. Sci. Rev.* 7(4), 737 (2020)
41. A. Gurarslan, Y. Yu, L. Su, Y. Yu, F. Suarez, S. Yao, Y. Zhu, M. Ozturk, Y. Zhang, and L. Cao, Surface-energy-assisted perfect transfer of centimeter-scale monolayer and few-layer MoS_2 films onto arbitrary substrates, *ACS Nano* 8(11), 11522 (2014)
42. X. Yuan, H. Liu, S. Liu, R. Zhang, Y. Wang, J. He, H. H. Tan, and C. Jagadish, Thermodynamic properties of metastable wurtzite InP nanosheets, *J. Phys. D* 54(50), 505112 (2021)
43. K. Zhang, C. Ding, B. Pan, Z. Wu, A. Marga, L. Zhang, H. Zeng, and S. Huang, Visualizing van der Waals epitaxial growth of 2D heterostructures, *Adv. Mater.* 33(45), 2105079 (2021)
44. S. Mukherjee, N. Nateghi, R. M. Jacobberger, E. Bouthillier, M. De La Mata, J. Arbiol, T. Coenen, D. Cardinal, P. Levesque, P. Desjardins, R. Martel, M. S. Arnold, and O. Moutanabbir, Growth and luminescence of polytypic InP on epitaxial graphene, *Adv. Funct. Mater.* 28(8), 1705592 (2018)
45. C. Sheng, Y. Bu, Y. Li, L. Su, Y. Yu, D. Cao, J. Zhou, X. Chen, W. Lu, and H. Shu, Phase-controllable growth of air-stable SnS nanostructures for high-performance photodetectors with ultralow dark current, *ACS Appl. Mater. Interfaces* 15(11), 14704 (2023)
46. H. Ryu, H. Park, J. H. Kim, F. Ren, J. Kim, G. H. Lee, and S. J. Pearton, Two-dimensional material templates for van der Waals epitaxy, remote epitaxy, and intercalation growth, *Appl. Phys. Rev.* 9(3), 031305 (2022)
47. D. Trots and S. Myagkota, High-temperature structural evolution of caesium and rubidium triiodoplumbates, *J. Phys. Chem. Solids* 69(10), 2520 (2008)
48. J. Liang, X. Han, J. H. Yang, B. Zhang, Q. Fang, J.

Zhang, Q. Ai, M. M. Ogle, T. Terlier, A. A. Martí, and J. Lou, Defect-engineering-enabled high-efficiency all-inorganic perovskite solar cells, *Adv. Mater.* 31(51), 1903448 (2019)

49. Y. Cheng, P. Tang, P. Liang, X. Liu, D. Cao, X. Chen, and H. Shu, Sulfur-driven transition from vertical to lateral growth of 2D SnS–SnS_2 heterostructures and their band alignments, *J. Phys. Chem. C* 124(50), 27820 (2020)
50. X. Liu, D. Cao, Y. Yao, P. Tang, M. Zhang, X. Chen, and H. Shu, Heteroepitaxial growth and interface band alignment in a large-mismatch $CsPbI_3$/GaN heterojunction, *J. Mater. Chem. C* 10(6), 1984 (2022)
51. H. Yuan, J. Su, S. Zhang, J. Di, Z. Lin, J. Zhang, J. Zhang, J. Chang, and Y. Hao, Interfacial transport modulation by intrinsic potential difference of Janus TMDs based on $CsPbI_3$/J-TMDs heterojunctions, *iScience* 25(3), 103872 (2022)
52. D. Guo, D. Bartesaghi, H. Wei, E. M. Hutter, J. Huang, and T. J. Savenije, Photoluminescence from radiative surface states and excitons in methylammonium lead bromide perovskites, *J. Phys. Chem. Lett.* 8(17), 4258 (2017)
53. A. Asaithambi, N. Kazemi Tofighi, N. Curreli, M. De Franco, A. Patra, N. Petrini, D. Baranov, L. Manna, F. D. Stasio, and I. Kriegel, Generation of free carriers in $MoSe_2$ monolayers via energy transfer from $CsPbBr_3$ nanocrystals, *Adv. Opt. Mater.* 10(14), 2200638 (2022)
54. X. Yang, S. Zhang, Z. Zhang, J. Lin, X. Liu, Z. Huang, L. Zhang, W. Luo, J. He, and X. Yuan, Controlled fabrication of $CsPbI_2Br$/transition metal dichalcogenide van der Waals heterostructure with fast carrier transfer process and interlayer exciton formation, *Physica E* 153, 115788 (2023)
55. M. Drüppel, T. Deilmann, P. Krüger, and M. Rohlfing, Diversity of trion states and substrate effects in the optical properties of an MoS_2 monolayer, *Nat. Commun.* 8(1), 2117 (2017)
56. T. Ye, J. Li, and D. Li, Charge-accumulation effect in transition metal dichalcogenide heterobilayers, *Small* 15(42), 1902424 (2019)
57. E. M. Alexeev, D. A. Ruiz-Tijerina, M. Danovich, M. J. Hamer, D. J. Terry, P. K. Nayak, S. Ahn, S. Pak, J. Lee, J. I. Sohn, M. R. Molas, M. Koperski, K. Watanabe, T. Taniguchi, K. S. Novoselov, R. V. Gorbachev, H. S. Shin, V. I. Fal'ko, and A. I. Tartakovskii, Resonantly hybridized excitons in moiré superlattices in van der Waals heterostructures, *Nature* 567, 81 (2019)
58. K. Ludwiczak, A. K. Dąbrowska, J. Binder, M. Tokarczyk, J. Iwański, B. Kurowska, J. Turczyński, G. Kowalski, R. Bożek, R. Stępniewski, W. Pacuski, and A. Wysmołek, Heteroepitaxial growth of high optical quality, wafer-scale van der Waals heterostrucutres, *ACS Appl. Mater. Interfaces* 13(40), 47904 (2021)
59. J. Li, X. Yuan, P. Jing, J. Li, M. Wei, J. Hua, J. Zhao, and L. Tian, Temperature-dependent photoluminescence of inorganic perovskite nanocrystal films, *RSC Advances* 6(82), 78311 (2016)
60. J. Lu, A. Carvalho, H. Liu, S. X. Lim, A. H. Castro Neto, and C. H. Sow, Hybrid bilayer WSe_2–$CH_3NH_3PbI_3$ organolead halide perovskite as a high-performance photodetector, *Angew. Chem.* 128(39), 12124 (2016)